

Wavefront engineering for controlled structuring of far-field intensity and phase patterns from multimodal optical fibers

Cite as: APL Photonics **6**, 051301 (2021); <https://doi.org/10.1063/5.0044666>

Submitted: 18 January 2021 • Accepted: 16 April 2021 • Published Online: 04 May 2021

 Liam Collard, Filippo Pisano, Marco Pisanello, et al.

COLLECTIONS

 This paper was selected as an Editor's Pick



[View Online](#)



[Export Citation](#)



CrossMark

ARTICLES YOU MAY BE INTERESTED IN

Observing distant objects with a multimode fiber-based holographic endoscope
APL Photonics 6, 036112 (2021); <https://doi.org/10.1063/5.0038367>

Wavefront shaping in multimode fibers by transmission matrix engineering
APL Photonics 5, 036103 (2020); <https://doi.org/10.1063/1.5136334>

Engineering interaction dynamics in active resonant photonic structures
APL Photonics 6, 050804 (2021); <https://doi.org/10.1063/5.0045228>

The image is a collage of various materials science applications and a large circular metallic component. The left side features a grid of material names and their applications, with a periodic table overlay. The right side shows a large, polished metallic ring.

Material	Application
sapphire windows	Nd:YAG
spintronics	raman substrates
silver nanoparticles	perovskites
MOCVD	barium borate
rare earth metals	quantum dots
osmium	scintillation Ce:YAG
refractory metals	laser crystals
anode	lithium niobate
dysprosium pellets	InAs wafers
chalcopyrite	ZnS
perovskite crystals	CdTe
yttrium iron garnet	glassy carbon
zeolites	III-V semiconductors
nano ribbons	barium fluoride
epitaxial crystal growth	ultra high purity materials
silver functionalized nanoparticles	cerium oxide polishing powder
cerium oxide polishing powder	transparent ceramics
europium phosphors	fused quartz
europium phosphors	beam splitters
europium phosphors	additive manufacturing
europium phosphors	organometallics
europium phosphors	infrared dyes
europium phosphors	CIGS
europium phosphors	nanodispersions
europium phosphors	cermet
europium phosphors	thin film
europium phosphors	100E grade materials
europium phosphors	QLED lighting
europium phosphors	solar energy
europium phosphors	sputtering targets
europium phosphors	fiber optics
europium phosphors	h-BN deposition slugs
europium phosphors	CVD precursors
europium phosphors	photovoltaics
europium phosphors	metamaterials
europium phosphors	borosilicate glass
europium phosphors	YBCO superconductors
europium phosphors	InGaAs
europium phosphors	indium tin oxide
europium phosphors	MgF ₂ rutile
europium phosphors	diamond micropowder
europium phosphors	optical glass

The Next Generation of Material Science Catalogs

Now Invent.™

www.americanelements.com
© 2001-2021, American Elements is a U.S. Registered Trademark

Wavefront engineering for controlled structuring of far-field intensity and phase patterns from multimodal optical fibers

Cite as: APL Photon. 6, 051301 (2021); doi: 10.1063/5.0044666

Submitted: 18 January 2021 • Accepted: 16 April 2021 •

Published Online: 4 May 2021



View Online



Export Citation



CrossMark

Liam Collard,^{1,a)}  Filippo Pisano,¹  Marco Pisanello,¹  Antonio Balena,^{1,2}  Massimo De Vittorio,^{1,2,a)}  and Ferruccio Pisanello^{1,a)} 

AFFILIATIONS

¹ Istituto Italiano di Tecnologia, Center for Biomolecular Nanotechnologies, Arnesano, LE 73010, Italy

² Dipartimento di Ingegneria Dell'Innovazione, Università del Salento, Lecce 73100, Italy

^{a)}Authors to whom correspondence should be addressed: liam.collard@iit.it; massimo.deVittorio@iit.it; and ferruccio.pisanello@iit.it

ABSTRACT

Adaptive optics methods have long been used to perform complex light shaping at the output of a multimode fiber (MMF), with the specific aim of controlling the emitted beam in the near field and enabling the realization of a new generation of endoscopes based on a wide variety of spectroscopic techniques. Gaining control of other emission properties, including the far-field pattern and the phase of the generated beam, would open up the possibility for multimode fibers to act as miniaturized multi-beam steering components and to implement phase-encoded imaging and sensing. In this study, we employ phase modulation using a spatial light modulator at the input of a multimode fiber to generate multiple, low divergence rays with controlled angles and phase at the fiber output. Direct measurement of the output angle and the divergence and phase of the generated beams show how wavefront engineering can be employed to perform complex far-field structuring of the emission of a MMF.

© 2021 Author(s). All article content, except where otherwise noted, is licensed under a Creative Commons Attribution (CC BY) license (<http://creativecommons.org/licenses/by/4.0/>). <https://doi.org/10.1063/5.0044666>

I. INTRODUCTION

Multimode optical fibers (MMFs) are intrinsically turbid media and the transmission of light through them is well known to scramble the phase and amplitude distribution of coherent light entering the proximal facet of the waveguide. As such, since the first demonstration of wavefront shaping through a highly scattering medium,¹ there has been significant interest in developing methods to deterministically pre-shape the phase of coherent light radiation, prior to transmission through the fiber, to control the emission patterns at the distal end. This approach has recently allowed the realization of low-invasiveness endoscopes based on a single imaging MMF.² Several adaptive optics methods have been applied to perform high-resolution imaging through wavefront modulation, including spatial light modulator (SLM) sub-domain optimization,³ SLM-based plane wave generation,^{4,5} digital micromirror device (DMD) phase optimization,⁶ digital phase conjugation,⁷ and a direct measurement of the transmission matrix of the MMF.⁸ All these approaches enable

structuring light emission in the vicinity of the fiber facet, e.g., in the near field. This has allowed for the development of a series of high-resolution imaging methods in transmission, reflection, fluorescence,⁹ Raman imaging¹⁰ and Coherent Anti-Stokes Raman Spectroscopy (CARS),^{11,12} optical manipulation,¹³ and through multicore fibers.¹⁴

Together with near-field structuring, engineering the far field of coherent light emitted from the MMF also has peculiar potentials. As the transmitted amplitude is scrambled, the same happens to output angles in the far field, resulting in speckle patterns. Therefore, structuring the far field emission offers interesting perspectives as the fiber output can be collimated at arbitrary angles within the fiber NA. This, in turn, paves the way for the exploitation of multimode fibers as passive beam-steering elements and beam splitting components in a miniaturized environment. For instance, optomechanical components such as microelectromechanical (MEMS) mirrors with sizes larger than an optical fiber could be substituted in miniaturized microscopes for neuroscience applications.¹⁵ Additionally,

direct monitoring of alterations in a structured far field transmitted through a MMF can reflect variations in the near-field environment at the MMF output and, for specifically designed claddings, those taking place around the waveguide, potentially enabling remote sensing applications with sensing elements placed either along the optical fiber or at its output.¹⁶ However, the control of MMF far-field phase and intensity patterns is typically achieved only with static methods by realizing complex meta-surfaces on the fiber facet.^{17,18} An adaptive method based on the use of a segmented deformable mirror has also been applied to explore the specific case of beam shaping through a ytterbium doped multimode fiber with gain in the far field,¹⁹ and re-configurable far-field space could also be obtained based on a computation of the measured transmission matrix through both distal and proximal fiber facets.⁸

In this study, we structure the far-field speckle pattern of a MMF, implementing spatially resolved phase modulation based on the plane wave optimization.⁴ The system is employed to tailor the output angle from the waveguide within its NA to generate multiple beams of low divergence angle emerging from the facet at different angles and to modulate their phase in a manner that is easily translatable into imaging applications. We provide a set of characterization data in the far-field plane that complement the existing reports in the near field, enabling further investigations to widen the potential applications of the technique.

II. EXPERIMENTAL METHODS

The implemented optical setup to control far-field emission patterns from a MMF is displayed in Fig. 1(a). A continuous wave 632 nm laser beam was expanded to overfill the 512×512 pixel screen of a SLM (ODP512, Meadowlark optics). The SLM phase pattern generated a scanning beam and a reference beam (hereafter referred to as B_{scan} and B_{ref}), both sent to lens L1 (focal length $f_{L1} = 200$ mm). A beam splitter (BS1), placed at 10 cm from L1, splits the optical path into a scan path (transmitted by BS1), which exploits B_{scan} , and a reference path (reflected by BS1), instead exploiting B_{ref} .

On the scan path, lenses L1 and L2 ($f_{L2} = 200$ mm) formed a 4f relay between the SLM and the back aperture of the microscope objective MO1 (0.65 NA, 40x, AMEP4625, ThermoFisher), while BS2 was used to image the input facet of the MMF onto a camera (CCD1). MO1 focused the beam onto a slack, ~5 cm-long MMF (0.22 NA, 50 μm core diameter, Thorlabs FG050UGA), which randomized the output pattern resulting in a new beam referred to as B_{random} . Light transmitted through the MMF was collected by the microscope objective MO2 (10x, 0.3 NA, MPLFLN10x—Olympus, $f_{MO2} = 18$ mm), and lenses L4 ($f_{L4} = 125$ mm) and L5 ($f_{L5} = 100$ mm) formed a 4f optical system conjugating the back focal plane of MO2 on CCD2 (CS505MU—Thorlabs), projecting on it the far field of the fiber facet (referred to as the (u, v) plane).

The distance r of a generic point (u, v) from the center of the far field is given by

$$r = \frac{f_{L5}}{f_{L4}} f_{MO2} \tan \theta_{out}, \quad (1)$$

where θ_{out} is the angle of the beam emitted by the fiber measured with respect to the optical axis, or in the component form, along the u and v axes, $u = \frac{f_{L5}}{f_{L4}} f_{MO2} \tan \theta_u$ and $v = \frac{f_{L5}}{f_{L4}} f_{MO2} \tan \theta_v$.

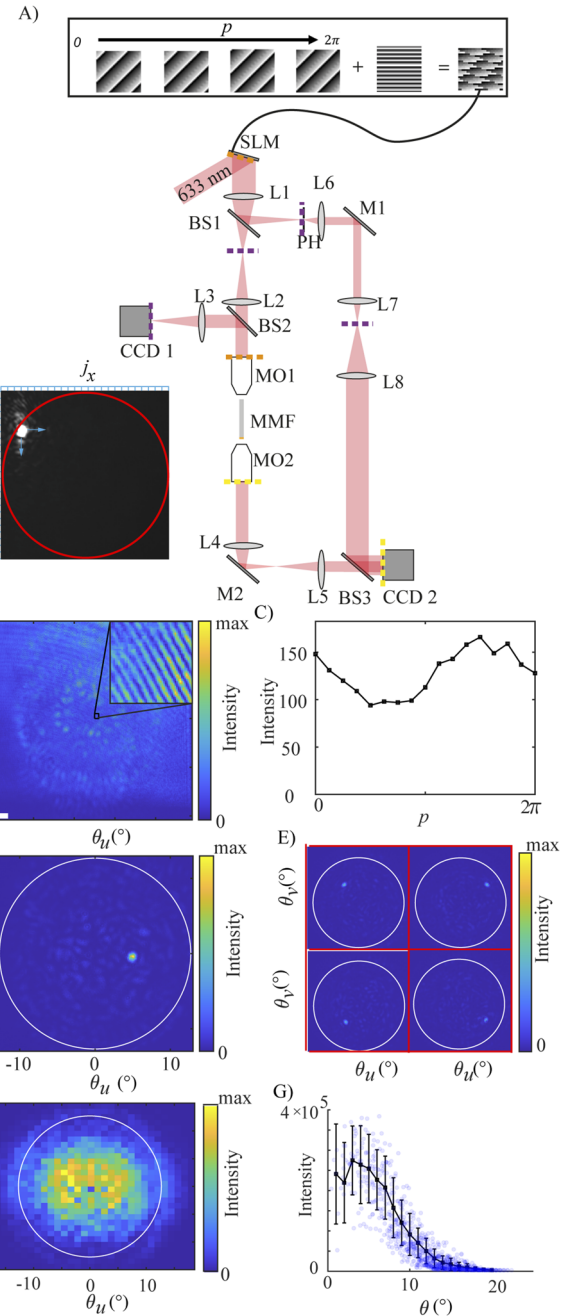


FIG. 1. (a) Optical system for direct far-field shaping of the MMF output: M—mirror, L—lens, MO—objective, MMF—multimode fiber, SLM—spatial light modulator, BS—beam splitter, and CCD—charged coupling device. Dashed lines indicate conjugate planes. Top inset: construction of the phase pattern displayed by the SLM to obtain B_{scan} and B_{ref} . Bottom left inset: indexing of the input facet of the MMF in a grid of 25×25 pixel elements. (b) Example interferogram $B_{\text{interfero}}^{j_x,j_y,p}$. (c) Intensity variation of $B_{\text{interfero}}^{j_x,j_y,p}$ at pixel (u, v) over the phase shift. (d) Image on CCD2 of a focused beam. (e) Images on CCD2 of different far-field foci (white circle indicates the theoretical limit of the fiber NA). (f) Focused beam intensity for each targeted far-field point. (g) Scatter plot of focused beam intensity (blue circles) and average focused beam intensity over 1° interval (black squares).

On the reference path, an adjustable iris was placed at the focal point of L1 blocking the residual scanning beam. B_{ref} was then expanded by a beam expander formed by lenses L7 and L8 ($f_{L7} = 30$ mm and $f_{L8} = 100$ mm) before being re-joined with the scanning beam by BS3. Thus, B_{random} and B_{ref} beams interfere on CCD2 with an angle controlled by BS3 [see the representative interferogram in Fig. 1(b)]. To obtain the B_{scan} and B_{ref} beams, blazed sawtooth gratings ϕ_{scan} and ϕ_{ref} were generated and summed together to obtain the image $\phi_{interfere}^{j_x,j_y,p}(x,y)$ on the SLM, whose screen plane is represented by x and y axes, with

$$\phi_{scan}^{j_x,j_y,p}(x,y) = \text{mod}(ax + by + p, 2\pi), \quad (2)$$

$$\phi_{ref}(x,y) = \text{mod}(cx, 2\pi), \quad (3)$$

where a and b define the periodicity of the grating along x and y so that the beam B_{scan} can scan on a 25×25 grid in the input facet of the MMF. Each element of this grid is identified by the indices (j_x, j_y) [see the bottom left inset of Fig. 1(a)]. The parameter c defines the periodicity of ϕ_{ref} , and it was chosen such that B_{ref} is aligned with the iris on the reference path and not on the core of the MMF along the scan path. Finally, p is the phase shift applied at each position in the (j_x, j_y) plane as detailed below.

To obtain a specific emission angle θ_{out} from the MMF, a plane wave calibration procedure was applied based on the method proposed in Ref. 3. In the algorithm, the (u, v) point related to a specific θ_{out} is monitored in intensity on the interference pattern on CCD2 while scanning the beam on the (j_x, j_y) plane using the following equation as an input to the SLM:

$$\phi_{interfere}^{j_x,j_y,p}(x,y) = \arg(\exp(i\phi_{scan}^{j_x,j_y,p}(x,y)) + \exp(i\phi_{ref})). \quad (4)$$

For each (j_x, j_y) pair, p was tested from 0 to 2π [the full scan procedure on the input facet is shown in visualization (1) of the supplementary material]. The intensity variation as a function of p on a representative (u, v) point of the far-field plane is displayed in Fig. 1(c), from which the phase step $p_{opt}^{j_x,j_y}$ giving the maximum intensity value at the coordinate (u, v) is extracted and used to generate the phase pattern for the $j_x^{\text{th}}, j_y^{\text{th}}$ grid element, $\phi_{opt}^{j_x,j_y}(x,y)$

$= \phi_{scan}^{j_x,j_y,p_{opt}^{j_x,j_y}}(x,y)$. This input-phase optimization procedure is repeated for all the 625 points on the (j_x, j_y) plane, generating the SLM input image to focus light on the point (u, v) of the far field, as given by the sum of all optimized phase patterns,

$$\Phi(x,y) = \arg\left(\sum_{j_x=1}^{25} \sum_{j_y=1}^{25} \exp(i\phi_{opt}^{j_x,j_y}(x,y))\right). \quad (5)$$

III. RESULTS AND DISCUSSION

Typical results of this optimization are shown in Figs. 1(d) and 1(e) for different (u, v) far-field points and in visualization 2 of the supplementary material. Once the fiber is bent or moved, Φ needs to be recomputed. Concerning computational times, for the 30×30 square array of focused spots in the (u, v) plane shown in visualization 2 of the supplementary material, the entire process

was completed within ~ 15 min. The majority of this time is dedicated to the computation of the optimized gratings on the graphics processing unit (GPU—NVIDIA GeForce GTX 960 in our case) and refreshing the SLM. On average, about 9% of the total intensity transmitted through the MMF is contained within the focused spot in the far field. This is comparable to what has been achieved in the near field,²⁰ although by applying polarization control, this could be further increased.³ In the near field, after removing lens L4, the intensity distribution appears to be stochastic and no trace of the far-field focus (shown in 1D) is visible (see Fig. S1 of the supplementary material).

A set of images of the 30×30 array of far-field spots [with the optical path in the configuration shown in Fig. 1(a)] were recorded on CCD2. The intensity of each far-field spot for each targeted pixel is shown as a color-map in Fig. 1(f), with related distribution displayed in Fig. 1(g). Although an overall decrease of intensity has been observed for high values of θ , the mean value of the beam waist remains much more stable across the entire fiber NA (see Fig. S2 of the supplementary material) although a small increase is observed close to the limit of the fiber (along the v axis, a 10% increase in average spot size was observed between spots generated at 0° and 12°). It has previously been demonstrated that in the near field, the signal to noise ratio increases at the edge of the fiber facet due to a higher availability of guided modes⁷—this is not the case when the system works in the far field. This can be likely assigned to the fact that the high order modes in the linearly polarized mode formulation ($LP_{l,m}$) are associated with a higher transversal component of the wavevector k_t and a lower power transfer efficiency.²¹ Indeed, as the number of modes available at a specific k_t increases for high order modes, a given position in the far field does not only foster the system working point at a specific k_t but also a specific pair (k_u, k_v) , being $k_t = \sqrt{k_u^2 + k_v^2}$. Recently, results showing a similar decrease in the intensity for lower values of θ have been reported for a DMD based calibration used to image distal objects from the fiber.²²

As the fiber length and bending could potentially influence the method, we investigated if far-field structuring is possible also for longer or bent fibers. Figures S3–S5 of the supplementary material show the distribution of beam intensity for a straight 5 cm fiber, a 5 cm-long fiber bent by 90° , and a 15 cm fiber, respectively. In these experiments, due to the changing position of the fiber, an internal reference beam was used to keep the reference signal preserved across different measurements and make them more comparable. In all three cases, more intense beams are generated at the center of the far field; however, beams of lower azimuthal angle generated through the 15 cm fiber appear to be of slightly weaker intensity than the 5 cm fiber. It is important to highlight, however, that the here-applied calibration procedure is sensitive to a dynamic deformation of the fiber. Although the transmission can be calibrated with the bent fiber, once the fiber is moved, a new calibration is required. Methods to compensate for bending have been investigated for near field optimizations,^{5,23} which could potentially be applied in our case. The guide star approach has been well established for focusing light through highly scattering media without prior knowledge of the distal side, with some approaches highlighted in Ref. 24, and recently applied to optical fibers.²⁵

To measure the azimuthal angle θ_{out} and the divergence angle α of the beam emitted by the fiber, MO2 was removed and a CCD (CS505MU—Thorlabs) fixed to a single axis translation stage

was positioned ~5 mm from the output of the MMF, as shown in Fig. 2(a). Thus, by measuring the profile of the speckle pattern (emitted directly from the fiber) in two positions (1 mm apart), θ_{out} and α could be estimated. Images of the beam in both CCD positions are shown in the inset of Fig. 2(a) (profile plots are shown in Fig. S6 of the [supplementary material](#)). Uncertainties were calculated by considering the distance between the two positions to be 1.0 ± 0.1 mm account for error in the position of CCD2.

To calculate θ_{out} , we considered the coordinate difference in the maximum intensity pixel for the first set (u_1, v_1) and second set (u_2, v_2) of images. For α , we consider the full width at half maximum (FWHM) of the intensity. Two example images of the speckle pattern emitted from the fiber in each position are shown in the inset of Fig. 2(a). The pixel size on the CCD was $3.45 \times 3.45 \mu\text{m}$, and therefore,

$$\theta_{out} = \tan^{-1} \left(\frac{3.45 \sqrt{(u_1 - u_2)^2 + (v_1 - v_2)^2}}{1000} \right), \quad (6)$$

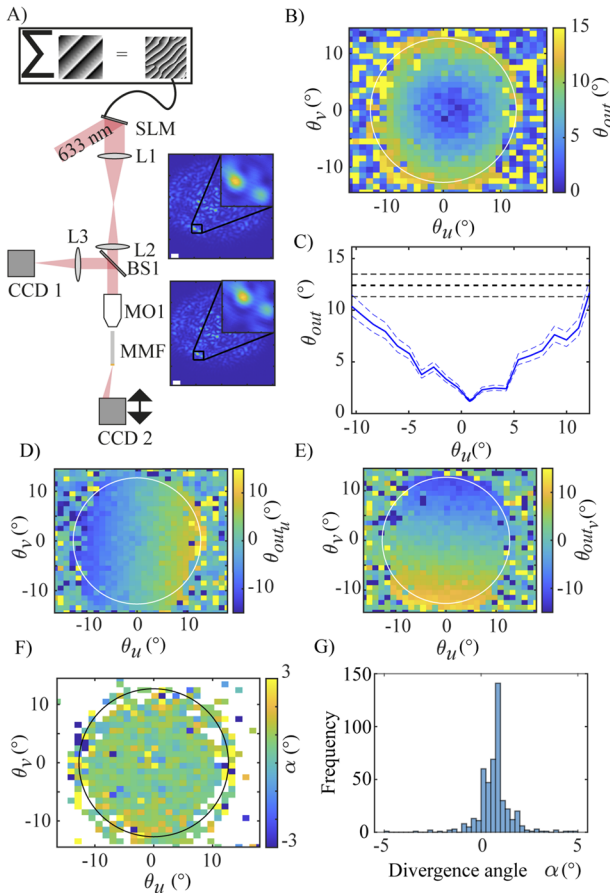


FIG. 2. (a) Optical setup to measure θ_{out} and α with CCD2 placed on a translation stage. (b) Measurement of θ_{out} for a 30×30 matrix of far-field foci. (c) Line plot of B—blue dashed lines indicate the error on θ_{out} . Black dashed lines indicate the theoretical limit from the fiber NA. [(d) and (e)] Measurement of θ_{out_u} and θ_{out_v} for a 30×30 matrix of far-field foci. (f) Measurement of divergence angle α for a 30×30 matrix of far-field foci. Points outside of the NA indicated in white (by setting a threshold on the intensity ratio of the far-field focus). (g) Histogram of α .

$$\alpha = 2 \tan^{-1} \left(\frac{3.45(FWHM_1 - FWHM_2)}{1000} \right). \quad (7)$$

Figure 2(b) is a color-map showing the measured θ_{out} for the targeted point of the (u, v) plane. As expected, at the center of the far field, the azimuthal angle is close to zero, whereas at the edge, θ_{out} approaches the limit of the numerical aperture of the fiber (NA = 0.22 corresponding to 12.7°). The relationship between the far field coordinate and the azimuthal angle is expected to follow (1). The experimental relationship between the far field coordinate and the measured θ_{out} is shown in the profile plot in Fig. 2(c). The angular components in the u and v directions are shown in Figs. 2(d) and 2(e), calculated as

$$\theta_{out_u} = \tan^{-1} \left(\frac{3.45(u_1 - u_2)}{1000} \right), \quad (8)$$

$$\theta_{out_v} = \tan^{-1} \left(\frac{3.45(v_1 - v_2)}{1000} \right). \quad (9)$$

The divergence angle α is plotted as a color-map in Fig. 2(f). The histogram of the data in Fig. 2(g) is shown in Fig. 2(g), featuring over 80% of the points between -1° and 1° (an average of 0.70° and a standard deviation of 0.68°). The low divergence angle and uniformity of the profile plots demonstrate that a far-field intensity structuring resulted in complex beam steering at the tip of a MMF.

After demonstrating how far-field beam steering of a laser beam can be performed through a MMF, next, we show how beam splitting may be performed to simultaneously generate n multiple beams f_{j_k} exiting the fiber with azimuthal angle θ_k . If $p_{opt}^{j_x j_y k}$ is the optimized phase shift for a given k^{th} far-field focus, with k ranging from 1 to n , the phase image on the SLM is then

$$\Phi(x, y) = \arg \left(\sum_{j_x=1}^{25} \sum_{j_y=1}^{25} \sum_{k=1}^n \exp(i\phi_{\text{scan}}^{j_x j_y} p_{opt}^{j_x j_y k}) \right). \quad (10)$$

Figure 3 shows the far-field image of three multiple beam arrays with 1, 2, and 3 different angles simultaneously. In this example, between 4% and 6% of the total intensity is contained in each hotspot array, with a signal to noise ratio reduced as the number of

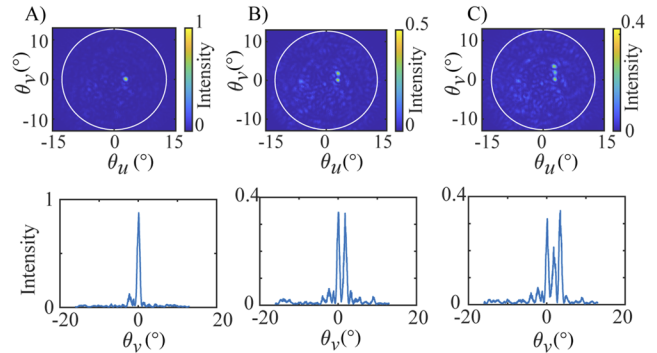


FIG. 3. Multiple far-field foci generated simultaneously and normalized profile plots (averaged over 20 pixels). (a) Single far-field focus. (b) Two far-field foci. (c) Three far-field foci.

beams is increased: the average beam intensity ($\frac{1}{n} \sum_{k=1}^n B_{\theta_k}$) falls from 1 to 0.5 to 0.39 and the signal to noise ratio falls from 268 to 132 to 108. Therefore, a far-field optimization of light transmission through a MMF can be used to perform complex beam steering of multiple beams, with the above-detailed limitations in terms of divergence angle and signal to noise ratio.

Another parameter that can be controlled by the optimization procedure is the phase of the outputted beam. So far, we have optimized the phase of the input beam to $p_{opt}^{j_x j_y}$, which gives the maximum intensity of the interference fringes at the targeted spot (u, v) , i.e., giving constructive interference between B_{ref} and B_{out} . However, it is also possible for B_{ref} and B_{out} to be out of phase by p , where p is in the range of $0-2\pi$. This can be done by applying a shift p to $p_{opt}^{j_x j_y}$, i.e., the phase is shifted by $q = \text{mod}(p_{opt}^{j_x j_y} + p, 2\pi)$. This gives an input phase image

$$\Phi_{phase}(x, y, p) = \arg \left(\sum_{j_x=1}^{25} \sum_{j_y=1}^{25} \exp(i\phi_{scan}^{j_x j_y, q}(x, y)) \right), \quad (11)$$

generating the beam $B_{phase}(p)$. To do this, 16 phase steps were applied to a single focused spot in the far-field plane. The intensity distribution is unaffected by the application of phase shift p . To measure the induced phase shift, the phase Ψ of $B_{phase}(p)$ was reconstructed from the Fourier transform of the interferogram between $B_{phase}(p)$ and B_{ref} .⁷ The interferogram and the reconstructed phase of B_{phase} for a representative value of $p = \pi$ are shown in Figs. 4(a) and 4(b), respectively.

Figure 4(c) shows the calculated phase shift $\Delta\Psi(p) = \Psi(B_{phase}(p)) - \Psi(B_{phase}(0))$. The linear fit of $\Delta\Psi(p)$ was $\Delta\Psi(p) =$

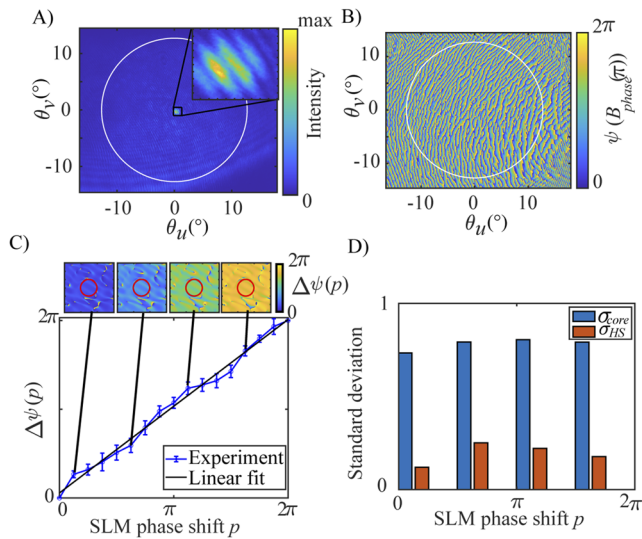


FIG. 4. (a) Interferogram between B_{ref} and B_{phase} . (b) Direct phase measurement of $B_{phase}(\pi)$ —circle indicates the limit of the NA of the fiber. (c) Top row: measurement of the phase shift between $B_{phase}(0)$ and $B_{phase}(p)$. $\Delta\Psi(p) = \Psi(B_{phase}(p)) - \Psi(B_{phase}(0))$: blue line is the experimental data and black line is a linear fit. (d) Bar graph showing the standard deviation of $\Delta\Psi(p)$ over the entire core (blue) and in the region corresponding to the far-field focus (orange).

$= 0.98p + 0.18$, indicating that the phase shift applied by the SLM was well preserved at the modulated beam emitted by the MMF. We have observed that this phase modulation takes place within the entire fiber NA, although the system provides a focused spot in a specific point of the far field, where the phase values are less dispersed than in the rest of the core [Fig. 4(d)].

IV. CONCLUSION

In summary, we report evidence that wavefront engineering techniques can be employed to achieve full control on the distribution of intensity and phase of light in the far field of a MMF. We have employed a plane wave based method, which complements other techniques such as the direct measurement of the transmission matrix,⁸ which could potentially be applied to control the far field transmission. Deep learning algorithms have also been applied to structure the near field without the need for any reference beam and could be investigated for the generation of low divergence rays.²⁶ Our results can potentially enable pure fiber-based beam steering of multiple collimated beamlets and open the door to the development of phase-encoded imaging and sensing through a MMF. Potentially, by adding a second fiber for collection, the weak scattering signal from distal objects is decoupled from the background signal from the fiber.

SUPPLEMENTARY MATERIAL

See the [supplementary material](#) for Figs. S1–S6.

ACKNOWLEDGMENTS

L.C., M.D.V., and Fe.P acknowledge funding from the European Union's Horizon 2020 Research and Innovation Program under Grant Agreement No. 828972. Fi.P., A.B., and Fe.P. acknowledge funding from the European Research Council under the European Union's Horizon 2020 Research and Innovation Program under Grant Agreement No. 677683. Fi.P., M.D.V. and Fe.P. acknowledge that this project has received funding from the European Union's Horizon 2020 Research and Innovation Program under Grant Agreement No 101016787. M.P. and M.D.V. acknowledge funding from the European Research Council under the European Union's Horizon 2020 Research and Innovation Program under Grant Agreement No. 692943. M.P., Fe.P., and M.D.V. were funded by the U.S. National Institutes of Health (Grant No. 1UF1NS108177-01). M.D.V. was funded by the U.S. National Institutes of Health (Grant No. U01NS094190).

M.D.V. and F.P. are founders and hold private equity in Optogenix, a company that develops, produces, and sells technologies to deliver light into the brain.

DATA AVAILABILITY

The data that support the findings of this study are available from the corresponding author upon reasonable request. The code used in this study will be made available at <https://www.projectnanobright.eu>.

REFERENCES

- ¹I. M. Vellekoop and A. P. Mosk, “Focusing coherent light through opaque strongly scattering media,” *Opt. Lett.* **32**, 2309–2311 (2007).
- ²T. Čižmár and K. Dholakia, “Exploiting multimode waveguides for pure fibre-based imaging,” *Nat. Commun.* **3**, 1027 (2012).
- ³T. Čižmár and K. Dholakia, “Shaping the light transmission through a multimode optical fibre: Complex transformation analysis and applications in biophotonics,” *Opt. Express* **19**, 18871–18884 (2011).
- ⁴M. Plöschner, B. Straka, K. Dholakia, and T. Čižmár, “GPU accelerated toolbox for real-time beam-shaping in multimode fibres,” *Opt. Express* **22**, 2933–2947 (2014).
- ⁵M. Plöschner, T. Tyc, and T. Čižmár, “Seeing through chaos in multimode fibres,” *Nat. Photonics* **9**, 529–535 (2015).
- ⁶A. M. Caravaca-Aguirre, E. Niv, D. B. Conkey, and R. Piestun, “Real-time resilient focusing through a bending multimode fiber,” *Opt. Express* **21**, 12881–12887 (2013).
- ⁷I. N. Papadopoulos, S. Farahi, C. Moser, and D. Psaltis, “Focusing and scanning light through a multimode optical fiber using digital phase conjugation,” *Opt. Express* **20**, 10583–10590 (2012).
- ⁸D. Loterie, S. Farahi, I. Papadopoulos, A. Goy, D. Psaltis, and C. Moser, “Digital confocal microscopy through a multimode fiber,” *Opt. Express* **23**, 23845–23858 (2015).
- ⁹S. A. Vasquez-Lopez, R. Turcotte, V. Koren, M. Plöschner, Z. Padamsey, M. J. Booth, T. Čižmár, and N. J. Emptage, “Subcellular spatial resolution achieved for deep-brain imaging *in vivo* using a minimally invasive multimode fiber,” *Light: Sci. Appl.* **7**, 110 (2018).
- ¹⁰I. Gusachenko, M. Chen, and K. Dholakia, “Raman imaging through a single multimode fibre,” *Opt. Express* **25**, 13782–13798 (2017).
- ¹¹A. Lombardini, V. Mytskanuk, S. Sivankutty, E. R. Andresen, X. Chen, J. Wenger, M. Fabert, N. Joly, F. Louradour, A. Kudlinski, and H. Rigneault, “High-resolution multimodal flexible coherent Raman endoscope,” *Light: Sci. Appl.* **7**, 10 (2018).
- ¹²J. Trägårdh, T. Pikálek, M. Šerý, T. Meyer, J. Popp, and T. Čižmár, “Label-free CARS microscopy through a multimode fiber endoscope,” *Opt. Express* **27**, 30055–30066 (2019).
- ¹³S. Bianchi and R. Di Leonardo, “A multi-mode fiber probe for holographic micromanipulation and microscopy,” *Lab Chip* **12**, 635–639 (2012).
- ¹⁴V. Tsvirkun, S. Sivankutty, K. Baudelle, R. Habert, G. Bouwmans, O. Vanvincq, E. R. Andresen, and H. Rigneault, “Flexible lensless endoscope with a conformationally invariant multi-core fiber,” *Optica* **6**, 1185–1189 (2019).
- ¹⁵W. Zong, R. Wu, S. Chen, J. Wu, H. Wang, Z. Zhao, G. Chen, R. Tu, D. Wu, Y. Hu, Y. Xu, Y. Wang, Z. Duan, H. Wu, Y. Zhang, J. Zhang, A. Wang, L. Chen, and H. Cheng, “Miniature two-photon microscopy for enlarged field-of-view, multi-plane and long-term brain imaging,” *Nat. Methods* **18**, 46–49 (2021).
- ¹⁶V. de Miguel Soto and M. Lopez-Amo, “Truly remote fiber optic sensor networks,” *J. Phys.: Photonics* **1**, 042002 (2019).
- ¹⁷A. Xomalis, I. Demirtzioglou, E. Plum, Y. Jung, V. Nalla, C. Lacava, K. F. MacDonald, P. Petropoulos, D. J. Richardson, and N. I. Zheludev, “Fibre-optic metadevice for all-optical signal modulation based on coherent absorption,” *Nat. Commun.* **9**, 182 (2018).
- ¹⁸N. Yu and F. Capasso, “Optical metasurfaces and prospect of their applications including fiber optics,” *J. Lightwave Technol.* **33**, 2344–2358 (2015).
- ¹⁹R. Florentin, V. Kermene, A. Desfarges-Berthelemot, and A. Barthélémy, “Shaping of amplified beam from a highly multimode Yb-doped fiber using transmission matrix,” *Opt. Express* **27**, 32638–32648 (2019).
- ²⁰R. di Leonardo and S. Bianchi, “Hologram transmission through multi-mode optical fibers,” *Opt. Express* **19**, 247–254 (2011).
- ²¹M. Pisanello, A. Della Patria, L. Sileo, B. L. Sabatini, M. de Vittorio, and F. Pisanello, “Modal demultiplexing properties of tapered and nanostructured optical fibers for *in vivo* optogenetic control of neural activity,” *Biomed. Opt. Express* **6**, 4014–4026 (2015).
- ²²I. T. Leite, S. Turtaev, D. E. Boonzaier Flaes, and T. Čižmár, “Observing distant objects with a multimode fiber-based holographic endoscope,” *APL Photonics* **6**, 036112 (2021).
- ²³D. Loterie, D. Psaltis, and C. Moser, “Bend translation in multimode fiber imaging,” *Opt. Express* **25**, 6263–6273 (2017).
- ²⁴R. Horstmeyer, H. Ruan, and C. Yang, “Guide-star-assisted wavefront-shaping methods for focusing light into biological tissue,” *Nat. Photonics* **9**, 563–571 (2015).
- ²⁵S. Li, S. A. R. Horsley, T. Tyc, T. Cizmar, and D. B. Phillips, “Guide-star assisted imaging through multimode optical fibres,” arXiv:2005.06445 [physics.optics] (2020).
- ²⁶B. Rahmani, D. Loterie, G. Konstantinou, D. Psaltis, and C. Moser, “Multimode optical fiber transmission with a deep learning network,” *Light: Sci. Appl.* **7**, 69 (2018).